PONTIFICIA UNIVERSIDAD CATÓLICA DE CHILE
ESCUELA DE INGENIERÍA

NOVEL TECHNIQUES AND SIGNAL MODELS WITH APPLICATIONS IN MRI

CARLOS CASTILLO PASSI

Thesis submitted to the Office of Research and Graduate Studies
in partial fulfillment of the requirements for the degree of
Master of Science in Engineering

Advisor:
PABLO IRARRÁZAVAL

Santiago de Chile, December 2018

PONTIFICIA UNIVERSIDAD CATÓLICA DE CHILE
ESCUELA DE INGENIERÍA

NOVEL TECHNIQUES AND SIGNAL MODELS WITH APPLICATIONS IN MRI

CARLOS CASTILLO PASSI

Members of the Committee:
PABLO IRARRÁZAVAL
CARLOS SING-LONG
AXEL OSSES
SERGIO MATURANA

Thesis submitted to the Office of Research and Graduate Studies
in partial fulfillment of the requirements for the degree of
Master of Science in Engineering

Santiago de Chile, December 2018

A mi familia y amigos por
apoyarme, aguantarme y
entenderme en este proceso.

ACKNOWLEDGMENTS

I have to give thanks to all the professors and people within the Electrical Engineering Department for constantly putting challenges, motivated and encouraged me to learn and improve in this field. I am very proud and grateful to have had the opportunity of being part of this Department and University, for giving me the possibility to grow as a researcher and as a person.

Also I want to mention, without any particular order, a few people for either inspire me or help me along the way in my career: José Lopez Tarres, Rafael Benguria, Christian Oberli, Angel Abusleme, Marjorie Oliveros and Mar Pérez-Sanagustín.

I would like to specially thank my advisor, Pablo Irrarázaval. Without him and his trust, the elaboration of these works would not have been possible.

Finally, I gratefully acknowledge CONICYT for funding this research through PIA-Anillo ACT1416.

CONTENTS

PART II. EFFECTIVE BARRIER SEPARATION FOR MICROSTRUCTURE ANALYSIS USING DSI

LIST OF FIGURES

LIST OF TABLES

PART I

GINI REWEIGHTED ℓ_1 MINIMIZATION FOR RAPID MRI

ABSTRACT

Undersampled acquisitions are often used to reduce the scan time in Magnetic Resonance Imaging (MRI). Compressed Sensing allows the reconstruction of the underlying image from this data by solving a convex optimization problem. This exploits the sparsity of the underlying image by using the ℓ_1-norm as a sparsity measure. This sparsity measure is key in the performance of the algorithm. In this work, we propose a method that uses the Gini Index (GI), a concept borrowed from economics, as a measure of sparsity for MR image reconstruction, since it satisfies all the desirable properties of a sparsity measure.

Because the GI is a quasi-convex function, the optimization problem can be solved by solving iteratively reweighted ℓ_1 problems. The algorithm was tested with a numerical phantom and *in vivo* MRI data. For the phantom, a perfect reconstruction was achieved using the GI with higher UnderSampling Factors (USFs) than with the traditional ℓ_1-norm. Improvements were also observed for the *in vivo* data**,** reducing the reconstruction error when using the GI which made possible to increase the USF by 0.5 with comparable error to the ℓ_1-norm.

The novelty of the proposed method is the application of the GI with complex data, undersampling and weak sparsity conditions, making it appropriate for many MRI applications, without an excessive computational load.

Keywords: Magnetic resonance imaging (MRI), Compressive sensing, Image reconstruction - iterative methods, Inverse methods.

RESUMEN

Las adquisiciones submuestreadas son comúnmente usadas para reducir el tiempo de escaneo en Imágenes por Resonancia Magnética (IRM). *Compressed Sensing* permite la reconstrucción de la imagen subyacente a partir de estos datos resolviendo un problema de optimización convexo. Este método explota la raleza de la imagen usando la norma-ℓ_1 como una medida de raleza. Esta medida es esencial en el desempeño del algoritmo. En este trabajo, proponemos un método que utiliza el Índice de Gini (IG), un concepto originado en economía, como una medida de raleza para la reconstrucción de IRM, debido a que satisface todas las propiedades deseables para una medida de raleza.

Debido a que el IG es una función cuasi-convexa, el problema de optimización es resuelto a través de resolver problemas ℓ_1 iterativamente pesados. Este algoritmo fue testeado en un fantoma numérico y con datos de IRM *in vivo*. Para el fantoma, una reconstrucción perfecta fue alcanzada usando el IG con Factores de SubMuestreo (FSM) más altos que la norma-ℓ_1. Mejoras fueron también observadas para los datos *in vivo*, reduciendo el error al usar el IG lo que hizo posible disminuir el FSM en 0.5 al comparar el error con la norma-ℓ_1.

La novedad del método propuesto es la aplicación del IG con datos complejos, submuestreo y condiciones débiles de raleza, haciéndolo apropiado para muchas aplicaciones en resonancia magnética, sin un excesivo aumento de la carga computacional.

Palabras Claves: Imágenes por resonancia magnética (IRM), *Compressive sensing*, Reconstrucción de imágenes - Métodos iterativos, Problemas inversos.

1. INTRODUCTION

In many MRI applications the acquisition speed is important, since it is related to the achievable spatial and temporal resolution, the spatial coverage, as well as making the acquisition less sensitive to motion. Therefore, many researches are focused on reducing the acquisition time without compromising image quality.

Undersampling k-space offers the possibility of shortening the scan time without degrading the image if an appropriate reconstruction method is used. Compressed Sensing (CS) (Candès & Wakin, 2008; Candès, Romberg, & Tao, 2006a, 2006b) is such a reconstruction method. It assumes that the image is compressible or sparse when represented in some domain, that is, the image can be represented with a few coefficients, in that domain. Mathematically this is described as having a small ℓ_0-norm. Since minimizing the ℓ_0-norm is a difficult problem, normally the ℓ_1-norm is used, and under certain conditions this will produce the same result. In particular the synthesis formulation of the basis pursuit denoising problem is the following

$$\begin{aligned} \mathrm{BP}_\epsilon) \quad \min_{\boldsymbol{\alpha}\in\mathbb{C}^N} \quad & \|\boldsymbol{\alpha}\|_1 \\ s.t. \quad & \|\Phi\Psi\boldsymbol{\alpha} - \boldsymbol{y}\|_2 \leq \epsilon, \end{aligned} \tag{I.1.1}$$

where $\Psi \in \mathbb{C}^{N\times N}$ is the sparse dictionary, $\Phi \in \mathbb{C}^{M\times N}$ is the undersampled Fourier matrix and $\boldsymbol{y} \in \mathbb{C}^M$ the acquired data. Then the recovered image is $\hat{\boldsymbol{x}} = \Psi\hat{\boldsymbol{\alpha}}$. The acceleration factor is inversely proportional to the Under Sampling Factor which we will call $\mathrm{USF} = N/M$.

In the standard formulation of CS, the ℓ_1-norm is used as a sparsity measure, but other measures of sparsity can be enforced (Hurley & Rickard, 2009). In this work we propose the use of the Gini Index (GI), an index used in economics to measure inequality, that has properties that could be useful in inverse problems.

2. THEORY

The GI is used in economics to measure inequality (Damgaard & Weiner, 2000). High inequality, where only a few have all the wealth is the kind of sparsity one would like to promote in the context of CS. We hypothesize that a formulation that maximizes the GI will produce good reconstructions for higher undersampling factors than conventional CS:

$$\begin{aligned} \max_{\boldsymbol{\alpha}\in\mathbb{C}^N} \quad & \mathrm{GI}\left(\boldsymbol{\alpha}\right) \\ s.t. \quad & \left\|\Phi\Psi\boldsymbol{\alpha}-\boldsymbol{y}\right\|_2 \leq \epsilon. \end{aligned}$$

The GI is defined as the mean of the differences between every possible pair of individuals, divided by the mean size (Damgaard & Weiner, 2000; Zonoobi, Kassim, & Venkatesh, 2011):

$$\mathrm{GI}\left(\boldsymbol{\alpha}\right) = \frac{\sum_{i=1}^{N}\sum_{j=1}^{N}\left||\alpha_i|-|\alpha_j|\right|}{2N\left\|\boldsymbol{\alpha}\right\|_1}. \tag{I.2.1}$$

If the data is sorted according to magnitude, (I.2.1) can be rewritten in a much simpler way. Let us define $\alpha_{[n]}$ to be the n-th element of the sorted vector $\boldsymbol{\alpha}$, $\left|\alpha_{[1]}\right| < \left|\alpha_{[2]}\right| < \ldots < \left|\alpha_{[N]}\right|$. Then, the definition in (I.2.1) can be applied to $\boldsymbol{\alpha}\in\mathbb{C}^N$ as in (Zonoobi et al., 2011; Huang, Shi, & Yan, 2015)

$$\mathrm{GI}\left(\boldsymbol{\alpha}\right) = 1-2\sum_{n=1}^{N}\underbrace{\left(\frac{N-n+\frac{1}{2}}{N}\right)}_{w_n}\frac{\left|\alpha_{[n]}\right|}{\left\|\boldsymbol{\alpha}\right\|_1} \tag{I.2.2}$$

$$= 1-2\left\|\frac{\boldsymbol{w}}{\left\|\boldsymbol{\alpha}\right\|_1}\odot\left(\mathcal{P}_{\boldsymbol{\alpha}}\boldsymbol{\alpha}\right)\right\|_1 \tag{I.2.3}$$

$$= 1-2\|\boldsymbol{W}_{\boldsymbol{\alpha}}\odot\boldsymbol{\alpha}\|_1, \tag{I.2.4}$$

where $\mathcal{P}_{\boldsymbol{\alpha}}$ is a permutation matrix that represents the sorting unitary operator ($\mathcal{P}_{\boldsymbol{\alpha}}\mathcal{P}_{\boldsymbol{\alpha}}^{\mathrm{T}}=\mathbb{I}$), $\boldsymbol{W}_{\boldsymbol{\alpha}}=\mathcal{P}_{\boldsymbol{\alpha}}^{\mathrm{T}}\boldsymbol{w}/\left\|\boldsymbol{\alpha}\right\|_1$ and $\boldsymbol{a}\odot\boldsymbol{b}$ is the Hadamard product or component-wise multiplication.

With this representation, the optimization becomes a weighted version of the denoised basis pursuit problem

$$\begin{aligned} \mathrm{BP}_\epsilon) \quad & \min_{\boldsymbol{\alpha}\in\mathbb{C}^N} \quad \|\boldsymbol{W}_{\boldsymbol{\alpha}} \odot \boldsymbol{\alpha}\|_1 \\ & s.t. \quad \|\Phi\Psi\boldsymbol{\alpha} - \boldsymbol{y}\|_2 \leq \epsilon. \end{aligned} \tag{I.2.5}$$

Hurley *et al.* showed that the GI satisfies all the desirable properties of a sparsity measure along with the $pq-$ mean (Hurley & Rickard, 2009) and it has been already used in inverse problems for image reconstruction of photography or radar images (Zonoobi et al., 2011; Feng, Xiao, & Wei, 2014), but it has never been used to reconstruct undersampled MRI data. Nevertheless, the proper mathematical background has not been fully developed yet, even though it is known that the GI is a quasi-convex function in $|\boldsymbol{\alpha}|$ (Zonoobi et al., 2011).

Zoonobi *et al.* (Zonoobi et al., 2011) solved this problem using the Simultaneous Perturbation Stochastic Approximation (SPSA) method, but they only considered $\boldsymbol{x} \in \mathbb{R}^N$ whereas in MRI the data is generally complex. Feng *et al.* (Feng et al., 2014) used the GI in a reweighted ℓ_1 scheme, trying to solve the inverse synthetic aperture radar (ISAR) imaging reconstruction. Their attempt explicitly included complex data and operators, but it was only tested in numerical phantoms. In both cases the optimization with the GI had better results compared with regular ℓ_1 optimization and also achieved perfect reconstruction for larger USFs (Zonoobi et al., 2011).

3. METHODS

3.1. Gini iteratively reweighted ℓ_1 algorithm

One of the problems for solving (I.2.5) is that the objective function is not convex and moreover it includes a sorting operation. As previously mentioned, Feng *et al*. (Feng et al., 2014) used an iteratively reweighted method where, for iteration k, the weights are $\boldsymbol{W}_{\boldsymbol{\alpha}^k} = \mathcal{P}^{\mathrm{T}}_{\boldsymbol{\alpha}^k}\boldsymbol{w}/\left\|\boldsymbol{\alpha}^k\right\|_1$. This enters in the category of an Iteratively Reweighted ℓ_1 (IRL1) algorithm proposed by Candès *et al*. (Candès, Wakin, & Boyd, 2008) in the family of methods to solve non-convex problems (Ochs, Dosovitskiy, Brox, & Pock, 2015). In contrast to previous works, since the factor $\left\|\boldsymbol{\alpha}^k\right\|_1$is constant for a particular iteration, our weight is just

$$\boldsymbol{W}_{\boldsymbol{\alpha}^k} = \mathcal{P}^{\mathrm{T}}_{\boldsymbol{\alpha}^k}\boldsymbol{w} \tag{I.3.1}$$

$$= \frac{N - \boldsymbol{I}^k + \frac{1}{2}}{N}, \tag{I.3.2}$$

with I^k_n the index of the sorted position of α^k_n such that $\left|\alpha^k_{[1]}\right| < \left|\alpha^k_{[2]}\right| < \ldots < \left|\alpha^k_{[N]}\right|$ and $\mathcal{P}_{\boldsymbol{\alpha}^k}$ a permutation matrix according to the sorting operation of $\boldsymbol{\alpha}^k$. Thus, the method will be equivalent to just a permutation of fixed weights $\boldsymbol{w}$ for every iteration k. This type of optimization problem and its properties are studied in (Huang et al., 2015; Bogdan, van den Berg, Sabatti, Su, & Candès, 2015). More importantly, this optimization method has been proven to converge in a finite number of iterations (Huang et al., 2015).

As for the effect of noise, we noticed an excessive variability in the weights. The performance of the reconstruction was dramatically improved when these weights were smoothed or denoised. The denoising was made by applying a median filter with an isotropic structural element of size 3 in each iteration, so the weights were

$$\tilde{\boldsymbol{W}}_{\boldsymbol{\alpha}^k} = \mathrm{medfilt}\left(\boldsymbol{W}_{\boldsymbol{\alpha}^k}\right), \tag{I.3.3}$$

interpreting $\boldsymbol{W}_{\boldsymbol{\alpha}^k}$ as a 2D image. As $\boldsymbol{\alpha}^k$ are the wavelet coefficients, the filtering enhanced the correlation in space of the weights and also reduced the noise that could be interpreted incorrectly as a feature of the image. As IRL1 methods are sensitive to the starting point, if a noisy weight is used, there is the risk of over-fitting to the noise. This effect was especially noticeable for USFs greater or equal to 4. With this filtering we slightly depart from the permutation of weights that justified the convergence of the method, but in practice gave more stable results.

In summary, we propose the following method:

Algorithm 1 Gini iteratively reweighted ℓ_1 algorithm

- **Initialization**: Choose $\boldsymbol{W}_{\boldsymbol{\alpha}^0} = 1$, so the result of the first iteration is the standard CS solution.
- **Update**: with $\boldsymbol{W}_{\boldsymbol{\alpha}^k} = \left(N - \boldsymbol{I}^k + \frac{1}{2}\right)/N$ as in (I.3.2) and $\tilde{\boldsymbol{W}}_{\boldsymbol{\alpha}^k}$ as (I.3.3) do

$$\boldsymbol{\alpha}^{k+1} = \underset{\boldsymbol{\alpha}\in\mathbb{C}^N}{\operatorname{argmin}} \|\tilde{\boldsymbol{W}}_{\boldsymbol{\alpha}^k} \odot \boldsymbol{\alpha}\|_1, \quad s.t. \quad \|\Phi\Psi\boldsymbol{\alpha} - \boldsymbol{Y}\|_2 \leq \epsilon.$$

Every weighted sub-problem in the algorithm can be solved either by using SPGL1 (van den Berg & Friedlander, 2007, 2008) or FISTA (Beck & Teboulle, 2009) (see Appendix), both implementations give the same result. For the data consistency tolerance ϵ, we chose it to be proportional to the standard deviation of the noise and inversely proportional to the square root of the under sampling factor (USF). The algorithm stops when the change in $\boldsymbol{\alpha}^k$ is small. It is considered small when the normalized root mean squared difference is between 1% and 5% (bigger for larger USFs).

3.2. Experimental setup

We tested the proposed reconstruction with a Shepp-Logan numerical phantom of size 256×256 and a radial undersampling pattern in the Fourier domain. The sparsifying transform was the Haar wavelet. We added complex noise in the Fourier domain with different Signal to Noise Ratios (SNRs), from $10\,\mathrm{dB}$ to $\infty\,\mathrm{dB}$. As we knew exactly the noise vector $\eta \in \mathbb{C}^N$, the data consistency constant ϵ was set as $\epsilon = \|U\eta\|_2$ with U the undersampling operator.

We also tested our algorithm with one *in vivo* data of the brain, acquired in a 3T Philips scanner. Acquisition parameters were: 2D T2W, $\mathrm{TSE} = 16$, size of 512×512, $\mathrm{NSA} = 4$, voxel size of $0.5/0.5/2\,\mathrm{mm}$, $\mathrm{FA} = 70\,\mathrm{deg}$, $\mathrm{TE} = 100\,\mathrm{ms}$, $\mathrm{TR} = 4000\,\mathrm{ms}$, and fully sampled acquisition.

For the reconstruction, we used retrospective undersampling with a variable density cartesian pattern. The sparsifying transform was the Daubechies wavelet (db8 with a decomposition level 8). A region of the background was used to estimate the noise $\eta_{\mathrm{BG}} \in \mathbb{C}^{N_{\mathrm{BG}}}$ and then a constant $\epsilon = K \left\| \frac{N}{N_{\mathrm{BG}}} \eta_{\mathrm{BG}} \right\|_2 / \sqrt{\mathrm{USF}}$ was used, with manually selected constant $K = 10$ as we underestimated the noise.

For the *in vivo* case, we also compared with a more popular weight $w_n = (|\alpha_n| + \gamma)^{-1}$ (Candès et al., 2008) which is related to solving the problem $\min_{\boldsymbol{x}} \sum_n \log(|\alpha_n| + \gamma)$, often used in IRL1 algorithms.

In this work the quality of the reconstructions were compared against the fully sampled gold standard using the Normalized Root Mean Squared Error (NRMSE), defined as

$$\mathrm{NRMSE}(\hat{\boldsymbol{x}}, \boldsymbol{x}) = \frac{\|\hat{\boldsymbol{x}} - \boldsymbol{x}\|_2}{\|\boldsymbol{x}\|_2}, \tag{I.3.4}$$

where $\hat{\boldsymbol{x}}$ is the reconstruction and $\boldsymbol{x}$ the ground truth, both in $\mathbb{C}^N$.

4. RESULTS AND DISCUSSION

4.1. Numerical phantom

As shown in Figure I.4.1, the proposed method obtained less error at all USFs and noise levels with SNR greater than $10\,\mathrm{dB}$. In the noise-free case ($\mathrm{SNR} = \infty\,\mathrm{dB}$), a perfect reconstruction was obtained for USFs up to 5 using the ℓ_1-norm and up to 5.5 using the GI (Figure I.4.2).

The GI sparsity showed greater improvements for higher USFs and for low levels of noise. The latter was expected since the noise effectively reduced the sparsity of the signal and, in that case, the sparsity measure was less relevant (Figure I.4.1).

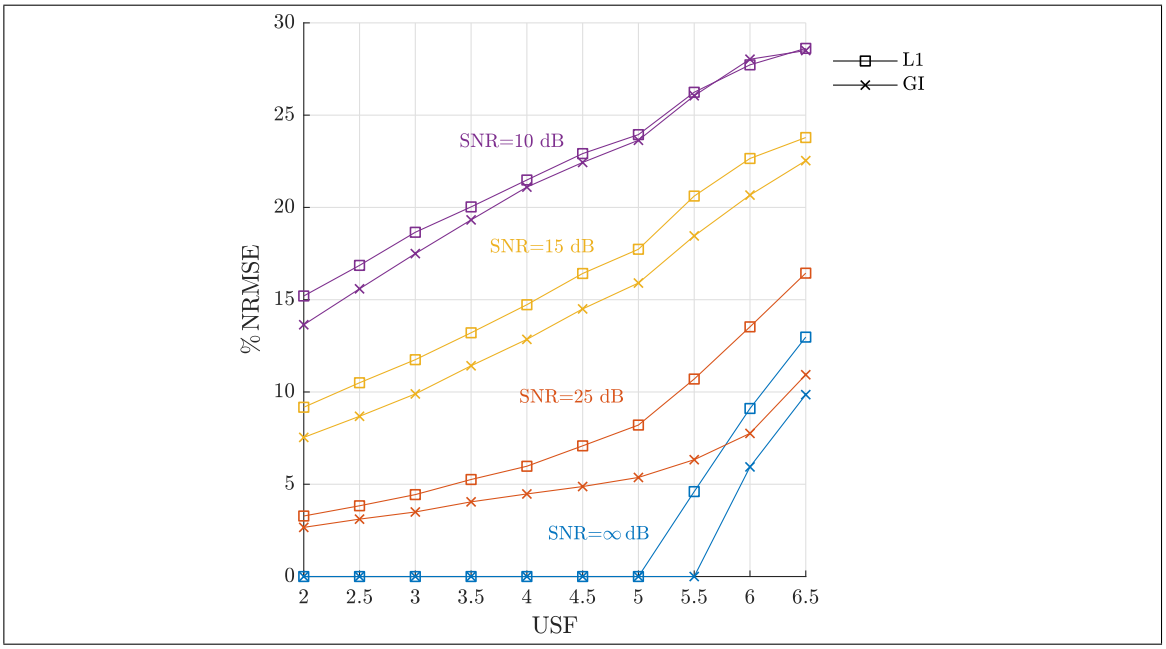

Figure I.4.1. NMRSE obtained for the phantom with the ℓ_1-norm and the GI reconstruction at different USFs and SNRs. Multiple SNRs in the range $10\,\mathrm{dB}$-$45\,\mathrm{dB}$ where tested, but just a few of them are shown for visual clarity.

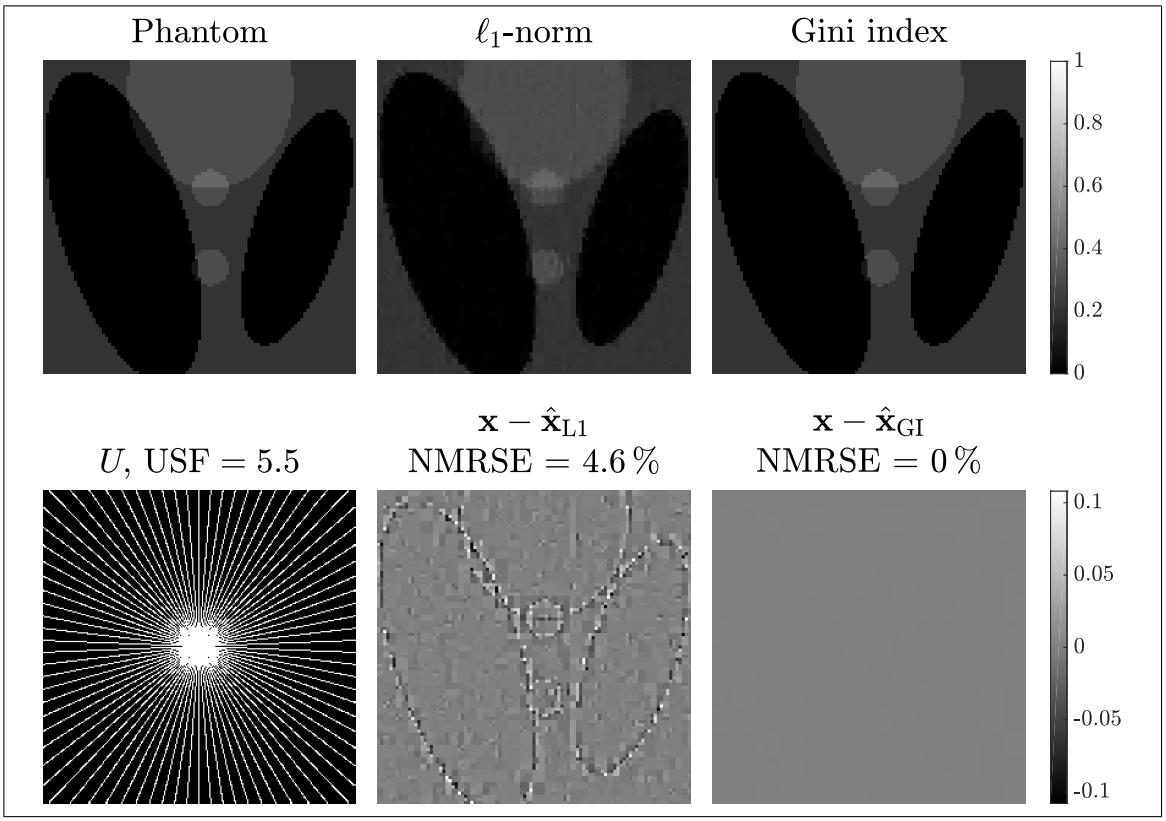

Figure I.4.2. Reconstruction for a Region Of Interest (ROI) of the phantom with the ℓ_1-norm and the GI sparsity measures at USF$= 5.5$ noise-free.

Tests were run in a computer with a Dual-Core Intel® Core™ i7-6500U CPU@2.50GHz. Using FISTA the reconstruction times were $3\,\mathrm{s}$ with three iterations and $1\,\mathrm{s}$ for CS. Most of the time three iterations were enough, but never more than eight. The reconstruction time using SPGL1 was approximately $200\,\mathrm{s}$. In contrast, the CS reconstruction took approximately $7\,\mathrm{s}$. As shown in Figure I.4.1, the improvement in reconstruction quality may be worth the extra reconstruction time.

4.2. *In vivo* MRI data

For the *in vivo* case, the reconstruction errors have the same behavior as for the numerical phantom. For undersampling factors between 2 and 5.5, the NRMSE was always

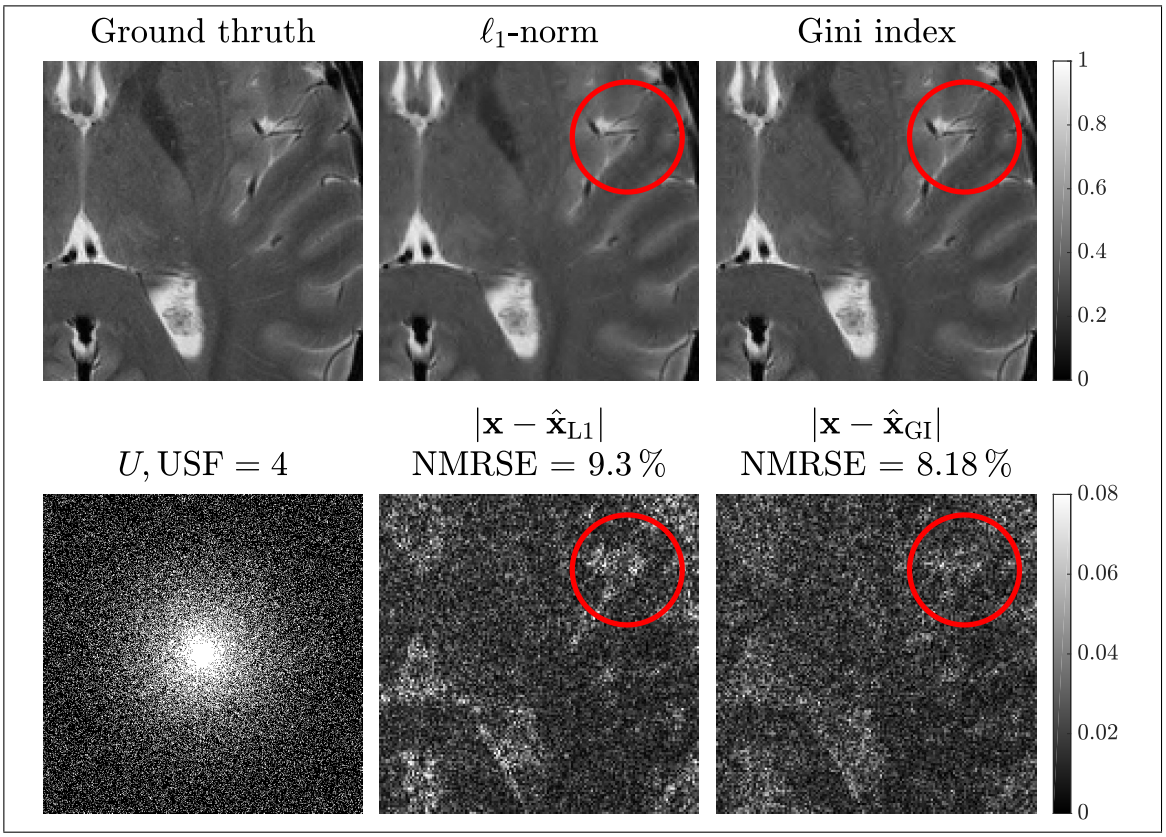

Figure I.4.3. Results for MRI data of a brain at an USF of 4. The errors in the obtained reconstructions is less for the GI measure of sparsity and the characteristics of the errors agree with the results obtained in the phantom, being less and most noticeable at the edges.

inferior when using the GI than using the ℓ_1-norm. The comparison was made in a Region Of Interest (ROI) that excludes the background (Figure I.4.4). The mean reduction of the NMRSE was $0.9\,\%$ in the tested range of USFs. It is interesting to note that with the GI one can achieve the same error as the ℓ_1-norm even with a 0.5 higher USF.

In Figure I.4.3 we show the results for the USF of 4 at a section of the ROI. The GI better preserved the edges of the image and the error was less localized when compared with the ℓ_1-norm.

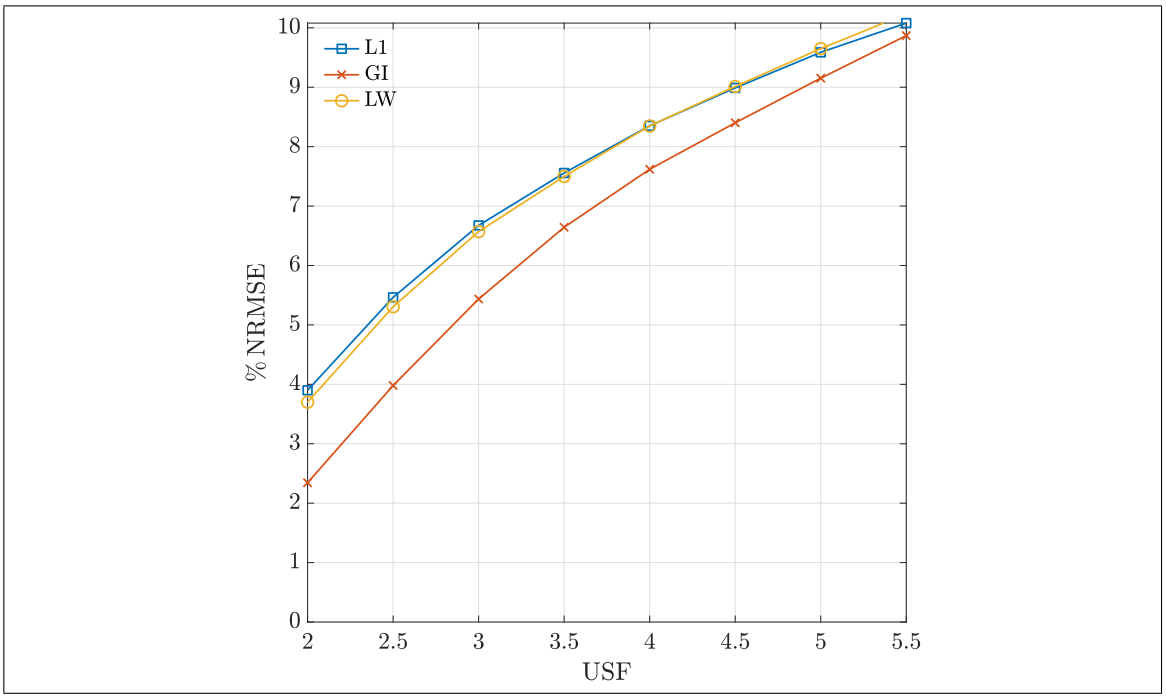

Figure I.4.4. Comparison between the ℓ_1-norm and the GI sparsity measures at different USFs for the MRI complex data. The log-weighted (LW) line make reference to weights of the form $w_n = (|\alpha_n| + \gamma)^{-1}$.

The reconstruction time using FISTA was approximately $21\,\mathrm{s}$ for three iterations. The CS reconstruction took approximately $7\,\mathrm{s}$. Using SPGL1 the reconstruction times were $530\,\mathrm{s}$ and $133\,\mathrm{s}$ respectively. The number of iterations was never more than three in this case.

The proposed method was also better than weights of the form $w_n = (|\alpha_n| + \gamma)^{-1}$(Candès et al., 2008) as shown in Figure I.4.4. The reconstruction times were comparable using FISTA.

5. CONCLUSIONS

Our hypothesis that using the GI will work better was validated by the results in this work. We achieved a reduction of the NRMSE in both the phantom and the *in vivo* case. For the phantom the reduction in error was significant, achieving a perfect reconstruction for a higher USF. For the *in vivo* image, an increase in the undersampling factor of 0.5 was possible with the same NRMSE as the ℓ_1-norm.

As the first iteration of the method is the standard CS, we provided a way to improve an already existing solution by doing consequent weighted ℓ_1 problems. The advantage of the proposed algorithm is that it is easy to implement with already existing codes for convex optimization as SPGL1 or FISTA using proximal operators to reduce the reconstruction time.

The filtering of the weights increased the reliability not only of the GI sparsity measure, but also is applicable for other IRL1 methods on problems with spatial correlation. Making them more robust to noise, undersampling and non ideal sparsity characteristics like the weak sparsity of natural images.

Future work should consider other ways of weight filtering, in particular, the denoising of the weights could vary between levels of decomposition for the wavelet basis and probably it is only necessary for higher levels (or more detailed basis). This algorithm could potentially improve the performance for other applications in MRI-related problems as SENSE, motion correction, etc.

REFERENCES

Beck, A., & Teboulle, M. (2009, January). A Fast Iterative Shrinkage-Thresholding Algorithm for Linear Inverse Problems. *SIAM Journal on Imaging Sciences*, *2*(1), 183–202. Retrieved 2017-09-11, from http://epubs.siam.org/doi/abs/10.1137/080716542 doi: 10.1137/080716542

Bogdan, M., van den Berg, E., Sabatti, C., Su, W., & Candès, E. J. (2015). Slope—adaptive variable selection via convex optimization. *The annals of applied statistics*, *9*(3), 1103–1140. Retrieved 2017-09-11, from http://www.ncbi.nlm.nih.gov/pmc/articles/PMC4689150/ doi: 10.1214/15-AOAS842

Candès, E. J., Romberg, J., & Tao, T. (2006a, February). Robust uncertainty principles: exact signal reconstruction from highly incomplete frequency information. *IEEE Transactions on Information Theory*, *52*(2), 489–509. doi: 10.1109/TIT.2005.862083

Candès, E. J., Romberg, J. K., & Tao, T. (2006b, August). Stable signal recovery from incomplete and inaccurate measurements. *Communications on Pure and Applied Mathematics*, *59*(8), 1207–1223. Retrieved 2017-09-11, from http://onlinelibrary.wiley.com/doi/10.1002/cpa.20124/abstract doi: 10.1002/cpa.20124

Candès, E. J., & Wakin, M. B. (2008, March). An Introduction To Compressive Sampling. *IEEE Signal Processing Magazine*, *25*(2), 21–30. doi: 10.1109/MSP.2007.914731

Candès, E. J., Wakin, M. B., & Boyd, S. P. (2008, December). Enhancing Sparsity by Reweighted l1 Minimization. *Journal of Fourier Analysis and Applications*, *14*(5-6), 877–905. Retrieved 2017-09-11, from https://link.springer.com/article/10.1007/s00041-008-9045-x doi: 10.1007/s00041-008-9045-x

Combettes, P. L., & Pesquet, J.-C. (2011). Proximal splitting methods in signal processing. In *Fixed-Point Algorithms for Inverse Problems in Science and Engineering* (pp. 185–212). Springer, New York, NY. Retrieved 2017-09-11, from https://link.springer.com/chapter/10.1007/978-1-4419-9569-8_10 (DOI: 10.1007/978-1-4419-9569-8_10)

Damgaard, C., & Weiner, J. (2000, April). Describing Inequality in Plant Size or Fecundity. *Ecology*, *81*(4), 1139–1142. Retrieved 2017-09-11, from http://onlinelibrary.wiley.com/doi/10.1890/0012-9658(2000)081[1139:DIIPSO]2.0.CO;2/abstract doi: 10.1890/0012-9658(2000)081[1139:DIIPSO]2.0.CO;2

Feng, C., Xiao, L., & Wei, Z.-H. (2014, August). Compressive Sensing Inverse Synthetic Aperture Radar Imaging Based on Gini Index Regularization. *International Journal of Automation and Computing*, *11*(4), 441–448. Retrieved 2017-09-11, from https://link.springer.com/article/10.1007/s11633-014-0811-8 doi: 10.1007/s11633-014-0811-8

Huang, X.-L., Shi, L., & Yan, M. (2015, June). Nonconvex sorted ell_1 minimization for sparse approximation. *Journal of the Operations Research Society of China*, *3*(2), 207–229. Retrieved 2017-09-11, from https://link.springer.com/article/10.1007/s40305-014-0069-4 doi: 10.1007/s40305-014-0069-4

Hurley, N., & Rickard, S. (2009, October). Comparing Measures of Sparsity. *IEEE Transactions on Information Theory*, *55*(10), 4723–4741. doi: 10.1109/TIT.2009.2027527

Ochs, P., Dosovitskiy, A., Brox, T., & Pock, T. (2015, January). On iteratively reweighted algorithms for nonsmooth nonconvex optimization in computer vision. *SIAM Journal on Imaging Sciences*, *8*(1), 331–372. Retrieved 2017-09-11, from http://epubs.siam.org/doi/abs/10.1137/140971518 doi: 10.1137/140971518

van den Berg, E., & Friedlander, M. (2008, November). Probing the Pareto Frontier for Basis Pursuit Solutions. *SIAM Journal on Scientific Computing*, *31*(2), 890–912. Retrieved 2017-09-11, from `http://epubs.siam.org/doi/abs/10.1137/080714488` doi: 10.1137/080714488

van den Berg, E., & Friedlander, M. P. (2007, June). *SPGL1: A solver for large-scale sparse reconstruction.* (http://www.cs.ubc.ca/labs/scl/spgl1)

Zonoobi, D., Kassim, A. A., & Venkatesh, Y. V. (2011, September). Gini Index as Sparsity Measure for Signal Reconstruction from Compressive Samples. *IEEE Journal of Selected Topics in Signal Processing*, *5*(5), 927–932. doi: 10.1109/JSTSP.2011.2160711

APPENDIX

A. PROXIMAL OPERATOR

When using the Fast Iterative Shrinkage Algorithm (FISTA) (Beck & Teboulle, 2009), every IRL1 sub-problem needs to be rewritten. Let us define $f(\boldsymbol{\alpha}) = \|\tilde{\boldsymbol{W}}_{\boldsymbol{\alpha}^k} \odot \boldsymbol{\alpha}\|_1$, then FISTA considers the following optimization problem

$$\boldsymbol{\alpha}^{k+1} = \underset{\boldsymbol{\alpha}\in\mathbb{C}^N}{\operatorname{argmin}}\, \lambda f(\boldsymbol{\alpha}) + \frac{1}{2}\|\Phi\Psi\boldsymbol{\alpha} - \boldsymbol{y}\|_2^2 . \tag{I.A.1}$$

Then, this formulation can be solved by using the proximal operator of the function f (Combettes & Pesquet, 2011; Huang et al., 2015)

$$\operatorname{prox}_{\lambda f}(\boldsymbol{\alpha}) = \max\left(|\boldsymbol{\alpha}| - \lambda\tilde{\boldsymbol{W}}_{\boldsymbol{\alpha}^k}, 0\right) \odot \operatorname{sign}(\boldsymbol{\alpha}), \tag{I.A.2}$$

with the sign of a complex number defined as $\operatorname{sign}(\alpha) = \alpha/|\alpha|$. In other words, $\operatorname{prox}_{\lambda f}(\boldsymbol{\alpha})$ is a soft thresholding of the coefficients $\boldsymbol{\alpha}$. Note that there always exist a λ that makes this formulation equivalent to the denoised basis pursuit.

PART II

EFFECTIVE BARRIER SEPARATION FOR MICROSTRUCTURE ANALYSIS USING DSI

ABSTRACT

MR Diffusion Spectral Imaging is an effective tool for obtaining relevant parameters from the tissue microstructure. This is particularly pertinent in the brain, for instance in estimating axon diameters. Current methods use strong assumptions about the geometry, shape and probability distributions. These assumptions limit their applicability in realistic and complex tissue. In this work we propose a new method to estimate what we call an effective barrier distribution by estimating the signal fraction of different barrier's sizes. In other words, we estimate the barrier distribution as a superposition of directional non-permeable barriers using a dictionary based method.

We tested the method with two phantoms: crossing fibers and a realistic corpus callosum with a distribution of axon diameters. The data was simulated with CAMINO with and without added noise. Our method was able to find a correct approximation of the barrier's separations. For the crossing fibers, the separations were estimated with standard deviation for each bundle of 1 and $1.6\,\mu\mathrm{m}$. For the corpus callosum phantom the normalized root mean square error of the signal fractions was $62\,\%$ due to inaccurate results for large barriers. As the separation increases the sensitivity is reduced, since the signal decays faster. Additionally, for large separations it gets more difficult to differentiate size, including free-diffusion.

This method allows to recover important information about the microstructure without the need of multiple acquisitions with different diffusion times. In the future we propose to include acceleration methods to acquire less q-space data points, and the use of other regularization functions.

Keywords: Diffusion MRI, Microstructure imaging, Convex optimization.

RESUMEN

Las IRM en difusión son una herramienta para obtener parámetros relevantes de la microestructura del tejido. Esto es particularmente atingente en el cerebro, al estimar el diámetro de los axones. Métodos actuales usan suposiciones acerca de la geometría, forma y densidad de probabilidad. En este trabajo proponemos un nuevo método para estimar lo que llamamos distribución de barreras efectiva estimando la fracción de señal de diferentes tamaños de barrera. En otras palabras, estimamos la distribución de barreras como una superposición de barreras direccionales y no permeables usando diccionarios.

Testeamos con dos fantomas: uno con fibras cruzadas y uno de cuerpo calloso con una distribución de diámetros de axones. Los datos fueron simulados con CAMINO con y sin ruido añadido. Nuestro método fue capaz de encontrar una aproximación correcta de la separación de barreras. Para las fibras cruzadas, la separación fue estimada con una desviación estándar de 1 y $1{,}6\,\mu\mathrm{m}$. Para el fantoma de cuerpo calloso el error cuadrático medio normalizado de las fracciones de señal fue $62\ \%$ debido principalmente a resultados poco precisos para las barreras más separadas. Cuando la separación incrementa la sensibilidad es reducida, debido a que la señal decae más rápido. Adicionalmente, para separaciones grandes se hace más difícil diferenciar los tamaños, incluyendo a la difusión libre.

Este método recupera información de la microestructura sin la necesidad de múltiples adquisiciones con distintos tiempos de difusión. En el futuro proponemos la inclusión de métodos de aceleración para tomar menos muestras en el espacio-q, y el uso de otras funciones de regularización.

Palabras Claves: IRM en difusión, Imágenes de microstructura, Optimización convexa.

1. INTRODUCTION

Diffusion MRI (dMRI) senses the diffusion of water molecules inside the microstructure (Stejskal & Tanner, 1965; Tanner & Stejskal, 1968) which affects the signal. Information obtained about axon morphometry by dMRI can give important insight about the functionality of the brain (Ritchie, 1982) and also about disorders such as multiple sclerosis and autism (Piven, Bailey, Ranson, & Arndt, 1997; Huang et al., 2016).

Several models and techniques have been proposed in the past to achieve this goal. In this work we focus on Diffusion Spectrum Imaging (DSI), a variation of dMRI with multiple gradient directions and strengths. There are several models to estimate the axon diameter for only one fiber direction: CHARMED (Assaf & Basser, 2005), AxCaliber (Assaf, Blumenfeld-Katzir, Yovel, & Basser, 2008), ActiveAx (Alexander et al., 2010), NODDI (Zhang, Schneider, Wheeler-Kingshott, & Alexander, 2012), the Minimal Model of White Matter Diffusion (MMWMD) and DIAMOND (Scherrer et al., 2013).

Every technique gives different ways to estimate parameters relevant to the microstructure. But, as the models are used to characterize the white matter, more strict assumptions should be made. A clear example is that the mentioned models do not consider more complex structures such as crossing fibers, which corresponds to $60\,\%$ to $90\,\%$ of the brain (Jeurissen, Leemans, Tournier, Jones, & Sijbers, 2013). Another common simplification, is to assume a gamma probability distribution for the axon diameters, even though studies of rat brains show that the distribution is more similar to a Generalized Extreme Value (GEV) (Sepehrband, Alexander, Clark, et al., 2016).

For multiple fiber directions, improvements to the reconstruction methods using optimization algorithms have been explored. They create dictionaries based on the models, to represent the signal and then minimize the ℓ_1 and ℓ_2-norms of the signal fractions, $\boldsymbol{f}$, for the different compartments. One example is the Accelerated Microstructure Imaging via Convex Optimization (Daducci et al., 2015) for regions with multiple fibers (AMICOx)

(Auría et al., 2015). And for models with more compartments: MMWMD (Sepehrband, Alexander, Kurniawan, Reutens, & Yang, 2016) and Microstructure Imaging of Crossing (MIX) white matter fibers (Farooq et al., 2016).

In this work, we propose a new flexible model based on non-permeable membranes, that removes the strong geometrical and distributional assumptions usually made about the microstructure.

2. THEORY

Diffusion Spectrum Imaging (DSI) acquires the Fourier transform of the Ensemble Average Propagator (EAP) (P. Callaghan, MacGowan, Packer, & Zelaya, 1991; P. T. Callaghan, 1993). This is obtained theoretically by first solving the diffusion equation. The problem of interest is to solve this equation for a non-permeable enclosure of separation a. The mathematical formulation of this phenomena for a particle positioned at x_0 is described by the following differential equation and boundary conditions

$$\begin{cases} \dfrac{\partial^2 p}{\partial x^2} = D\dfrac{\partial p}{\partial \Delta} \\ p\left(x,0\right) = \delta\left(x - x_0\right) \\ \dfrac{\partial p}{\partial x}\left(x,\Delta\right) = 0 \qquad\qquad x \in \left\{0,a\right\}, \end{cases}$$

where p is the probability density distribution, D the diffusion coefficient and a the separation between barriers. By solving this equation we obtain the propagator for a given initial position of the particle x_0

$$\begin{aligned} p_{x_0}\left(x\right) = \frac{1}{a} \sqcap \left(\frac{x - a/2}{a}\right) \\ \times \left[1 + 2\sum_{n=1}^{\infty} \cos\left(\frac{n\pi}{a}x\right) \cos\left(\frac{n\pi}{a}x_0\right) e^{-D\Delta(n\pi/a)^2}\right]. \end{aligned} \tag{II.2.1}$$

After applying the ensemble average, assuming a uniform distribution of particles in space, we get what is known as the Ensemble Average Propagator (EAP)[1]. Then, for the Pulsed Gradient Spin Echo (PGSE) sequence together with the short pulse approximation (that the gradient separation Δ is much larger than the length δ or $\Delta \gg \delta$), we can relate the signal $E\left(q\right)$ with the Fourier transform of the EAP. The signal $E\left(q\right)$ is written in terms of the q-space formalism, with $q = \frac{\gamma}{2\pi}\delta G$, γ the gyromagnetic constant and G the diffusion gradient strength. Finally we obtain the Tanner signal equation for an impermeable barrier

[1]Defining the Ensemble Average Propagator as $p\left(r\right) = \int \rho\left(x_0\right) p_{x_0}\left(r + x_0\right) \mathrm{d}x_0$, with $\rho\left(x_0\right)$ the density of spins in the position x_0. For uniformly distributed spins the expression becomes $p\left(r\right) = \frac{1}{a}\int_0^a p_{x_0}\left(r + x_0\right) \mathrm{d}x_0$.

of separation a (Stejskal & Tanner, 1965)

$$E_{\bar{\Delta},a}(q) = \sum_{n=0}^{\infty} (2 - \delta[n])\, e^{-D\bar{\Delta}(n\pi/a)^2} \frac{\operatorname{sinc}^2\left(aq + \frac{n}{2}\right)}{\left(1 - n\,(2aq)^{-1}\right)^2}, \tag{II.2.2}$$

with $\bar{\Delta} = \Delta - \delta/3$ the diffusion time[2]and Δ/δ the separation/duration of the diffusion gradients. To visualize the effect of the barrier size on the signal in (II.2.2), the results for different barrier separations are shown in Figure II.2.1.

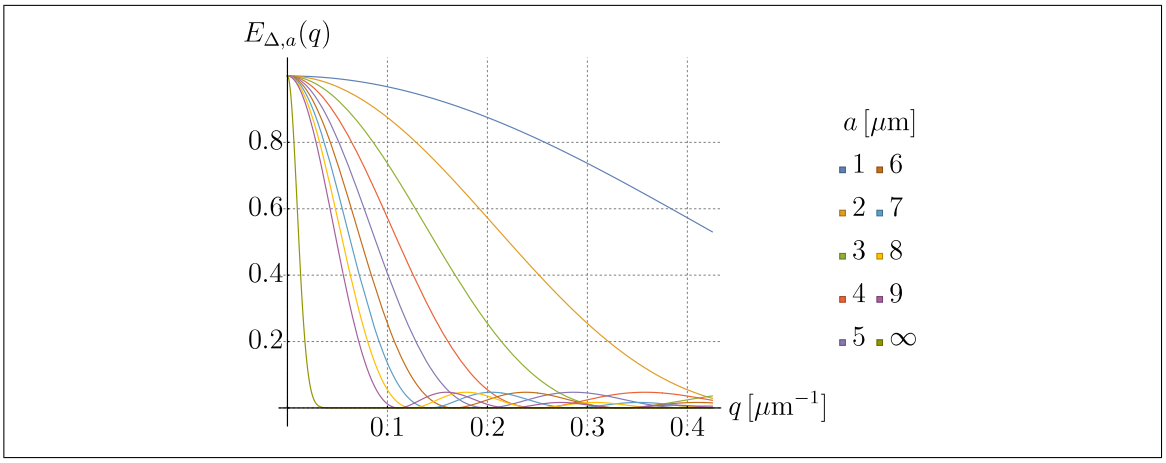

Figure II.2.1. Signal for different barrier separations a, between $1\,\mu$m and $9\,\mu$m also including free diffusion ($a \to \infty$), with $\Delta/\delta = 70/10\,\mathrm{ms}$, $D = 2 \cdot 10^{-9}\,\mathrm{m}^2/\mathrm{s}$ and $G_{\max} = 1000\,\mathrm{mT/m}$.

For the case of permeable barriers with permeability μ, a closed expression can also be obtained (Yablonskiy & Sukstanskii, 2010)

$$E_{\Delta,a,\mu}(\tilde{q}) = \frac{(2\tilde{q})^2}{\tilde{\mu}} \sum_k \frac{e^{-D\Delta(n_k/a)^2} n_k^2 \sin n_k}{(\tilde{q}^2 - n_k^2)\left((2\tilde{\mu}+1)\sin n_k + n_k \cos n_k\right)},$$

[2]To simplify notation, we will call the diffusion time just Δ from now on, and Δ will only mean diffusion gradient separation if it is in a parameter pair like Δ/δ.

where $\tilde{q} = aq$, $\tilde{\mu} = a\mu/D$ and the summation is over all non-negative roots n_k of the transcendental equation

$$2\tilde{\mu}\left(\cos n - \cos \tilde{q}\right) - n \sin n = 0. \tag{II.2.3}$$

Given that the solution of (II.2.3) can only be obtained numerically or by approximations, a simplification for the long-time regime $\Delta D/a^2 \gg 1$ (highly constrained when compared to the displacement) can be made (Yablonskiy & Sukstanskii, 2010; Sukstanskii, Yablonskiy, & Ackerman, 2004)

$$E_{\Delta,a,\mu}\left(q\right) \approx \operatorname{sinc}^2\left(aq\right) \exp\left(-4\sin^2\left(aq\right)\frac{\mu\Delta}{a}\right). \tag{II.2.4}$$

For the case of non-permeable barriers ($\mu = 0$) the approximation becomes

$$E_{\Delta,a}\left(q\right) \approx \operatorname{sinc}^2\left(aq\right). \tag{II.2.5}$$

This expression can be interpreted intuitively as if each propagator (II.2.1) will not depend on the initial position x_0 and therefore $p_{x_0}\left(r\right) \approx \frac{1}{a} \sqcap \left(\frac{r}{a}\right)$. Thus, the ensemble average will be just an auto-correlation of the compartment shape, and the diffusion signal is obtained by using the correlation property of the Fourier transform

$$\begin{aligned} p_{x_0}\left(r\right) \star p_{x_0}\left(r\right) &= \frac{1}{a} \sqcap \left(\frac{r}{a}\right) \star \frac{1}{a} \sqcap \left(\frac{r}{a}\right) \\ &\xrightarrow{\mathcal{F}} \operatorname{sinc}^2\left(aq\right). \end{aligned}$$

This result is also applicable to higher dimensions and it has been used to estimate axon diameters under long diffusion times $\Delta \to \infty$ (Sanguinetti & Deriche, 2014).

3. METHODS

3.1. Effective barrier separation

We will introduce the concept of an effective barrier separation a as the separation between planar and uniformly spaced barriers. Our hypothesis is that we can superimpose many of these bundles to correctly approximate the true signal $E(q)$. This can be done in one given diffusion direction or in many directions. We will call the weights of these superpositions: directional signal fraction, $f_i = f(a_i)$ for one diffusion direction and total signal fraction or simply signal fraction, f_{ij} for multiple diffusion directions.

The signal for a bundle of evenly spaced planes at separation a_0, evaluated at an angle θ with respect to the barrier normals is for the long-time regime

$$E(\boldsymbol{q}) = E_{\Delta,a_0}(q\cos\theta)\, E_{\Delta,\infty}(q\sin\theta) \tag{II.3.1}$$

$$\overset{\Delta D/a^2 \gg 1}{=} \operatorname{sinc}^2(a_0 q\cos\theta)\exp\left(-4\pi^2\Delta D\,(q\sin\theta)^2\right). \tag{II.3.2}$$

Because of the free diffusion term, parallel to the barriers, this formula cannot be easily interpreted in an angular manner. Nevertheless, the first two terms of its Taylor expansion, do represent rotations that can be used to obtain angular information.

$$\begin{aligned} E(\boldsymbol{q}) &= \left(1 - \frac{1}{3}(\pi a_0 q\cos\theta)^2 + \dots\right)\left(1 - 4\Delta D\,(q\sin\theta)^2 + \dots\right) \\ &= 1 - \frac{1}{3}(\pi q)^2 \underbrace{\left[(a_0\cos\theta)^2 + (a_{\text{free}}\sin\theta)^2\right]}_{a^2} + \dots \\ &\approx \operatorname{sinc}^2(aq), \end{aligned} \tag{II.3.3}$$

with $a_{\text{free}} = 2\sqrt{3\Delta D}$ a free diffusion effective barrier size and

$$a = \sqrt{(a_0\cos\theta)^2 + (a_{\text{free}}\sin\theta)^2} \tag{II.3.4}$$

the effective barrier separation.

Then, we propose that at any diffusion gradient direction $\hat{\boldsymbol{n}}_j$, the microstructure can be represented as a superposition of barriers with directional signal fractions f_i or

$$y\left(q\right) = f_\infty E_{\Delta,\infty}\left(q\right) + \sum_{i=1}^{M-1} f_i E_{\Delta,a_i}\left(q\right)$$

$$\boldsymbol{y} = \mathrm{E}\left(\boldsymbol{a}, \boldsymbol{q}, \boldsymbol{\Delta}\right)\boldsymbol{f}, \tag{II.3.5}$$

with $E_{\Delta,\infty}\left(q\right) = \exp\left(-4\pi^2 q^2 D\Delta\right)$ the free diffusion signal, $E_{\Delta,a_i}\left(q\right)$ the restricted diffusion signal and a_i barrier sizes uniformly sampled between arbitrary selected $a_{\min}$ and $a_{\max}$.

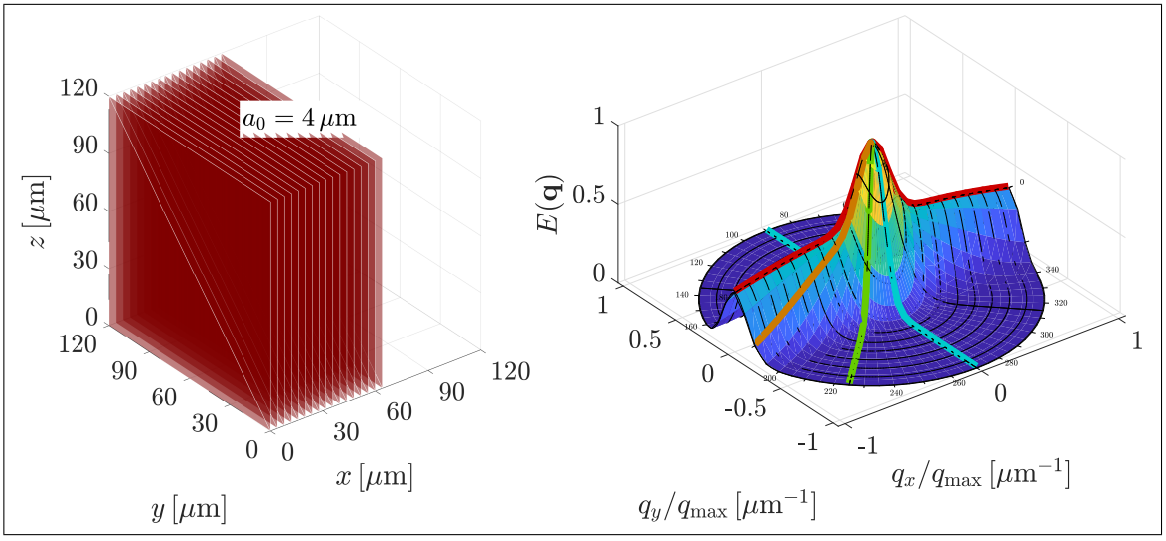

Figure II.3.1. (Left.) Barrier bundle with barriers with separations of $4\,\mu$m at an angle of $0\,\mathrm{deg}$. (Right.) Diffusion signal obtained for the microstructure, sampled in a disk on the $q_x - q_y$ plane. In red the signal for a diffusion gradient in the direction $\theta = 0\,\mathrm{deg}$, in orange for $\theta = 10\,\mathrm{deg}$, in green for $\theta = 45\,\mathrm{deg}$ and in cyan for $\theta = 90\,\mathrm{deg}$. The central peak is almost entirety due to free diffusion.

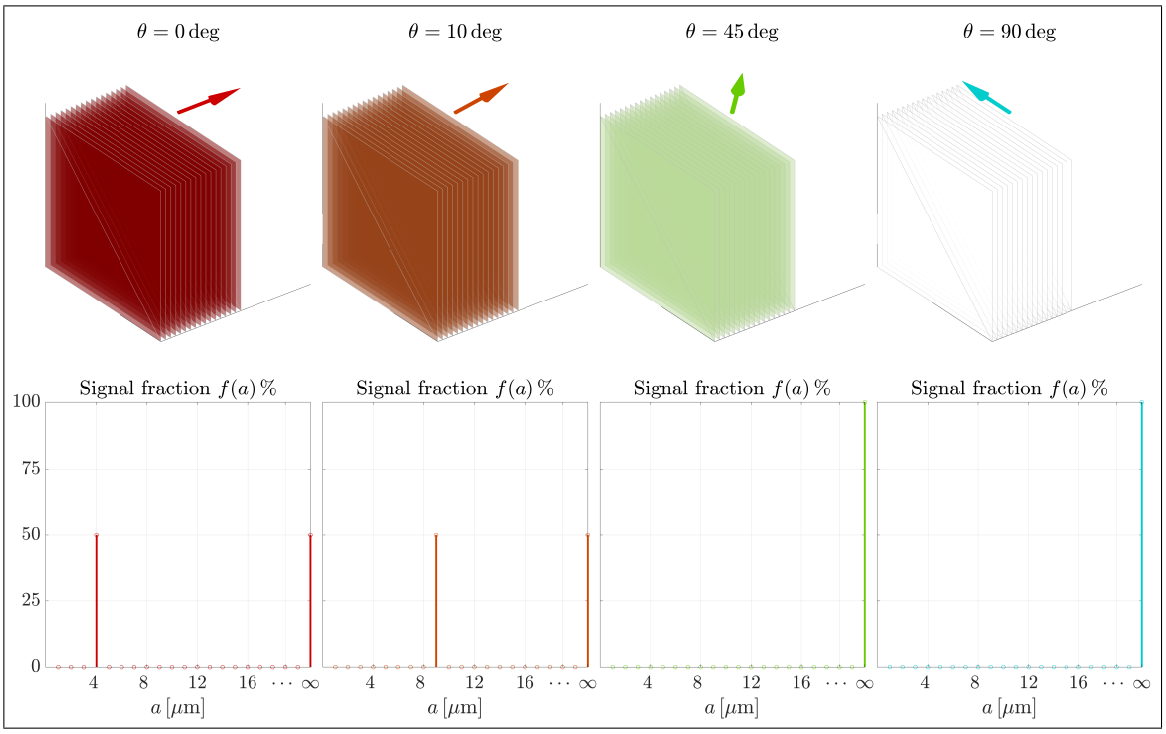

Figure II.3.2. As the diffusion gradient direction change (the colored arrow), the signal will change also and therefore the equivalent barrier distribution. Due to the acquisition parameters, there will be a point in which the signal of a sufficiently big barrier bundle will not be distinguishable from free diffusion.

For example, lets consider the simple case of a voxel with half free and half barriers as shown in Figure II.3.1. At the right of the same sub figure, we show different directions of encoding. Each of these directions generates a signal shown angularly. These signals can be expressed as the sum of two effective barriers (one of them free diffusion) with the directional signal fractions as shown in Figure II.3.2. There will be a barrier size large enough such that the signal is no longer distinguishable from free diffusion either for the acquisition parameters Δ/δ or because of the SNR (Sepehrband, Alexander, Kurniawan, et al., 2016).

It is worth noting that this does not only work for planes, for example, for cylinders the peak in the directional signal fractions will change from a delta to a wider distribution.

The effective barrier can be related also with the cylinder diameter by multiplying by a compensation factor

$$a_{\text{cyl}} = 2/\sqrt{3}\, a, \tag{II.3.6}$$

obtained using the Taylor series of $E_{\text{cyl}}(q) = 2\dfrac{J_1(a_{\text{cyl}}\pi q)}{a_{\text{cyl}}\pi q}$, similarly to (II.3.3).

3.2. Optimization method

As a non-permeable barrier distribution in every direction $\boldsymbol{f}_j \in \mathbb{R}^M$ can effectively characterize any geometry, this gives us a general model without strong assumptions in the angular correlation of $\boldsymbol{f}_j$ (geometry) or the distribution of those in the given direction (probability distribution).

For this type of analysis it is common to use a multi-shell acquisition (Figure II.3.3). In general, we can use N shells of radius $\boldsymbol{q} = \frac{\gamma}{2\pi}\boldsymbol{\delta} \odot \boldsymbol{G} \in \mathbb{R}^N$ ($\odot$ is the component-wise mutltiplication) with different diffusion times $\boldsymbol{\Delta} \in \mathbb{R}^N$ and pulse widths $\boldsymbol{\delta} \in \mathbb{R}^N$. Now, if we use the notation $E_{n,m} = E_{\Delta_n, a_m}(q_n)$, for every direction we have

$$\begin{aligned}
\mathrm{E}\boldsymbol{f}_j &= \left[\begin{array}{ccc|c} E_{1,1} & \cdots & E_{1,M-1} & E_{1,\infty} \\ E_{2,1} & \cdots & E_{2,M-1} & E_{2,\infty} \\ E_{3,1} & \cdots & E_{3,M-1} & E_{3,\infty} \\ \vdots & \vdots & \vdots & \vdots \\ E_{N,1} & \cdots & E_{N,M-1} & E_{N,\infty} \end{array}\right] \left[\begin{array}{c} f_1 \\ f_2 \\ \vdots \\ f_{M-1} \\ f_\infty \end{array}\right]_j \\
&= \Big[\underbrace{\boldsymbol{E}_{\boldsymbol{\Delta},1}(\boldsymbol{q}) \quad \cdots \quad \boldsymbol{E}_{\boldsymbol{\Delta},M-1}(\boldsymbol{q})}_{\text{Restricted}} \;\Big|\; \underbrace{\boldsymbol{E}_{\boldsymbol{\Delta},\infty}(\boldsymbol{q})}_{\text{Free}}\Big]\, \boldsymbol{f}_j.
\end{aligned}$$

The acquisition parameters $\boldsymbol{\Delta}/\boldsymbol{\delta}$ could have a different value per shell, which allow us to modify the SNR per shell (Alexander et al., 2010).

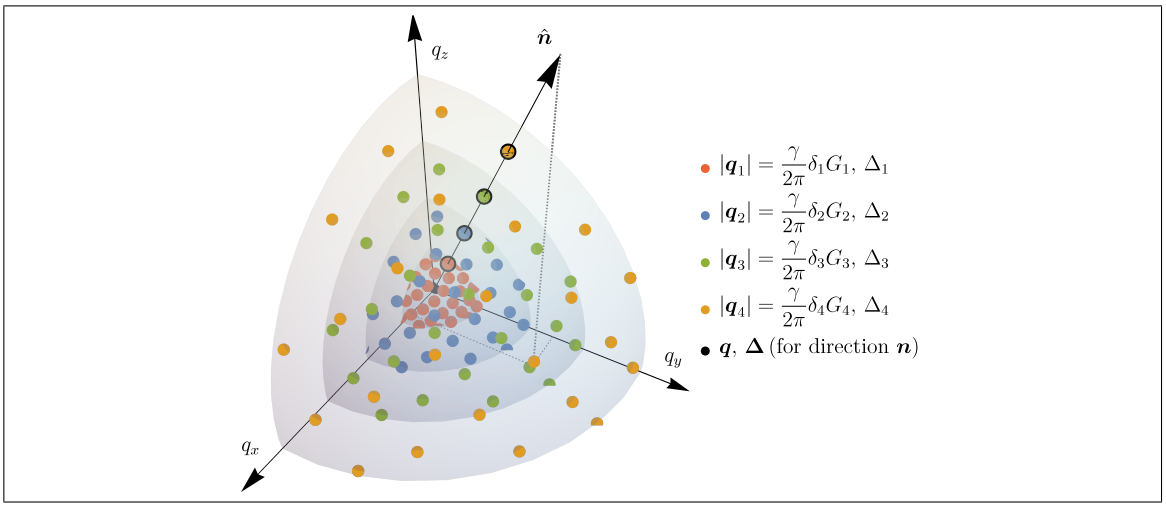

Figure II.3.3. Example of a multi-shell q-space sampling for $N = 4$ shells. The Δ/δ parameters could potentially change between shells.

Finally, we propose to solve the following optimization problem

$$\begin{aligned} \min_{f \in \mathbb{R}_{[0,1]}} \quad & \sum_j \left\| \boldsymbol{f}_j \right\|_1 + \lambda \left\| \boldsymbol{f}_{\infty,j} \right\|_2^2 \\ s.t. \quad & \left\| \mathrm{E}\boldsymbol{f}_j - \boldsymbol{y}_j \right\|_2^2 \leq \epsilon, \quad \forall j \\ & \left\| \boldsymbol{f}_j \right\|_1 = 1, \quad \forall j, \end{aligned}$$

with E the matrix with the barrier signals defined in Equation II.2.2 (including free diffusion, but not considering permeability), $\boldsymbol{f}_j$ the signal fractions and $f_{\infty,j}$ the free diffusion component for the diffusion gradient direction $\hat{\boldsymbol{n}}_j$. The rationale behind using an additional norm for the free diffusion was to avoid overfitting to those atoms of the dictionary, since those contribute more to the overall signal. This problem was solved using CVX (Grant & Boyd, 2008, 2014).

3.3. Experiments

The proposed method was tested with synthetic data created with CAMINO (Hall & Alexander, 2009). For the first experiment, crossing bundles were used (Figure II.3.4) with $N_{\text{spins}} = 5 \cdot 10^4$, $T = 10^3$, $D = 2 \cdot 10^{-9}\,\text{m}^2/\text{s}$, $G_{\max} = 1700\,\text{mT/m}$ and $\Delta/\delta = 100/1\,\text{ms}$. For the second experiment, a more realistic corpus callosum phantom with gamma distributed cylinders was used (Figure II.4.4). As this microstructure is more complex, more computationally demanding parameters were used $N_{\text{spins}} = 10^5$, $T = 2 \cdot 10^3$ and $D = 1.7 \cdot 10^{-9}\,\text{m}^2/\text{s}$. For the acquisition parameters $G_{\max} = 1000\,\text{mT/m}$ and $\Delta/\delta = 70/8\,\text{ms}$ were used.

Both experiments were tested for the noise-free case and with Rician noise of standard deviation σ,

$$E = \left| E_{\text{true}} + \eta_1 + i\,\eta_2 \right|, \quad \eta_1, \eta_2 \sim \mathcal{N}(0, \sigma)\,.$$

The q-space sampling were multiple semi-disks in the $q_x - q_y$ plane, constituted by 32 uniformly spaced directions and radii.

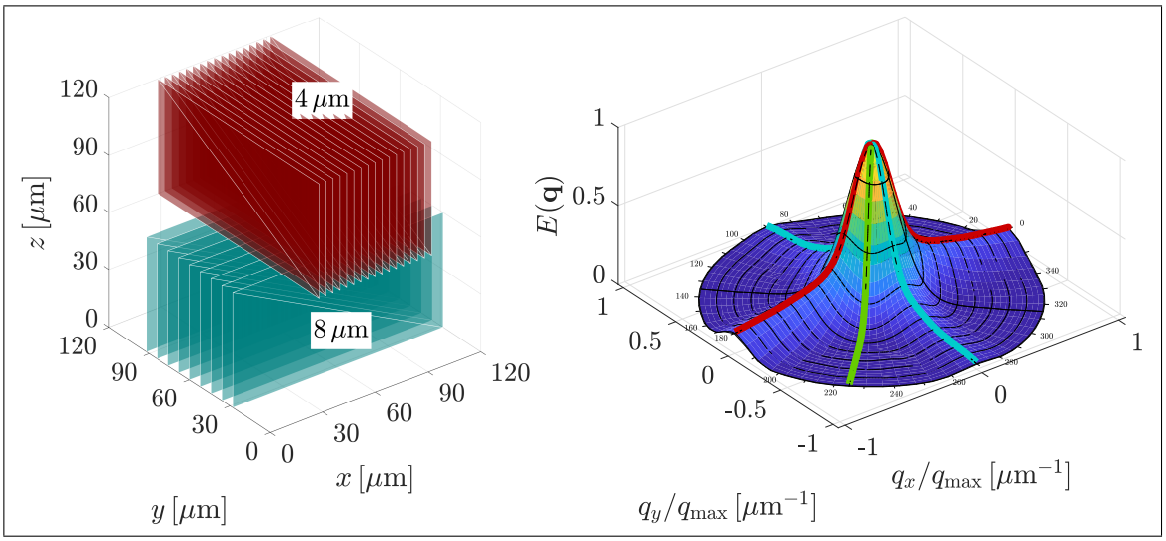

Figure II.3.4. (Left.) Crossing fibers phantom with a barrier bundle of separations of $4\,\mu$m and $8\,\mu$m. (Right.) Signal produced by the phantom of crossing fiber, in red the signal for a diffusion gradient direction of $\theta = 0\,\text{deg}$, in green for $\theta = 45\,\text{deg}$ and in cyan for $\theta = 90\,\text{deg}$.

4. RESULTS AND DISCUSSION

4.1. Crossing fibers

The results for the noiseless case shown in Figure II.4.1 approximate well the microstructure in Figure II.3.4.

Even though the signal fractions should be delta distributions in the correct barrier sizes this is not possible for two reasons. The first is that the correct barrier size is not necessarily sampled. In this case the closest were $4.5\,\mu\mathrm{m}$ and $8\,\mu\mathrm{m}$. And the second, due to the acquisition parameters, like q-space sampling or noise, is that there are limits on the resolution for a. The maximum barrier size $a_{\max}$ has a high signal fraction, because it is similar to free diffusion and can compensate some errors in the estimation of the constant $D\Delta$. While the position of the peaks are very close to the ground truth, the signal fractions are not necessarily correct as the atoms $\{E_{\Delta,a_i}\}_{i=1,..,M-1}$ are not linearly independent and it is always possible to attribute contributions of smaller separation barriers to bigger ones. Different types of barrier sampling and weighting were tested to tackle this problem, but they did not improved the results considerably. We can also see a close relation between the effective barrier separation in Equation II.3.4 and the results seen in Figure II.4.2. For more than one barrier, the effective barrier was calculated using $a = \min\left\{\left\|(4\,\mu\mathrm{m}, a_{\mathrm{free}}) \odot \hat{\boldsymbol{n}}_1\right\|, \left\|(8\,\mu\mathrm{m}, a_{\mathrm{free}}) \odot \hat{\boldsymbol{n}}_2\right\|\right\}$, with $\hat{\boldsymbol{n}}_k$ the unitary normal vector to the barrier bundles.

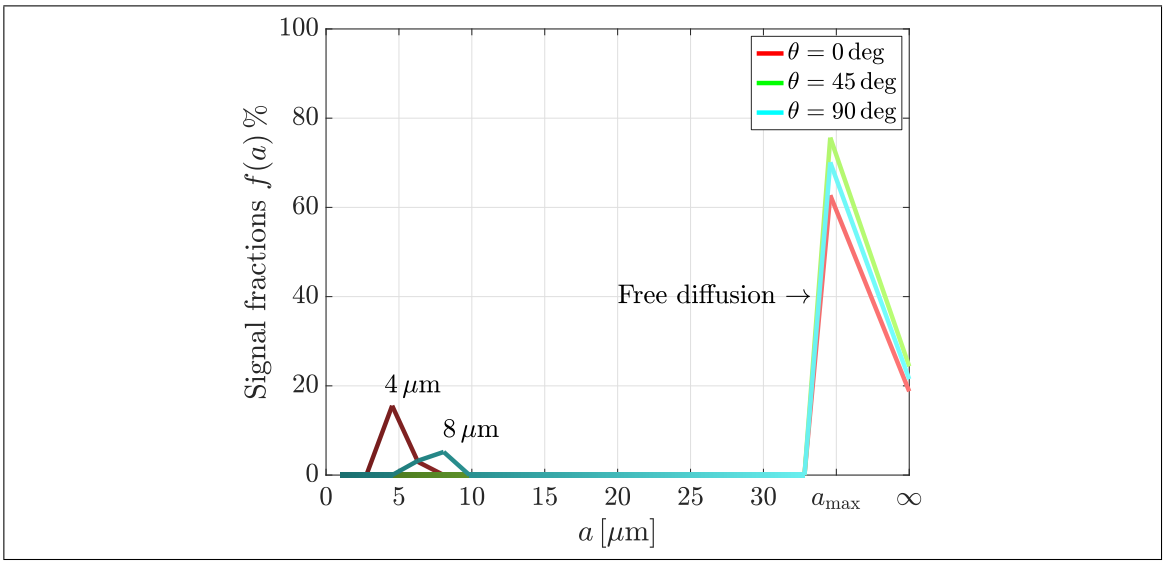

Figure II.4.1. Signal fractions obtained by the proposed method for a noise-less signal for multiple diffusion gradient directions as stated in Figure II.3.4. The signal fractions peak near the corresponding barrier separations $4\,\mu\text{m}$ at $\theta = 0\,\text{deg}$ and $8\,\mu\text{m}$ at $\theta = 90\,\text{deg}$. The used parameters were $\epsilon = 3\%$, $\sigma = 0\%$ and $\lambda = 10^{-3}$.

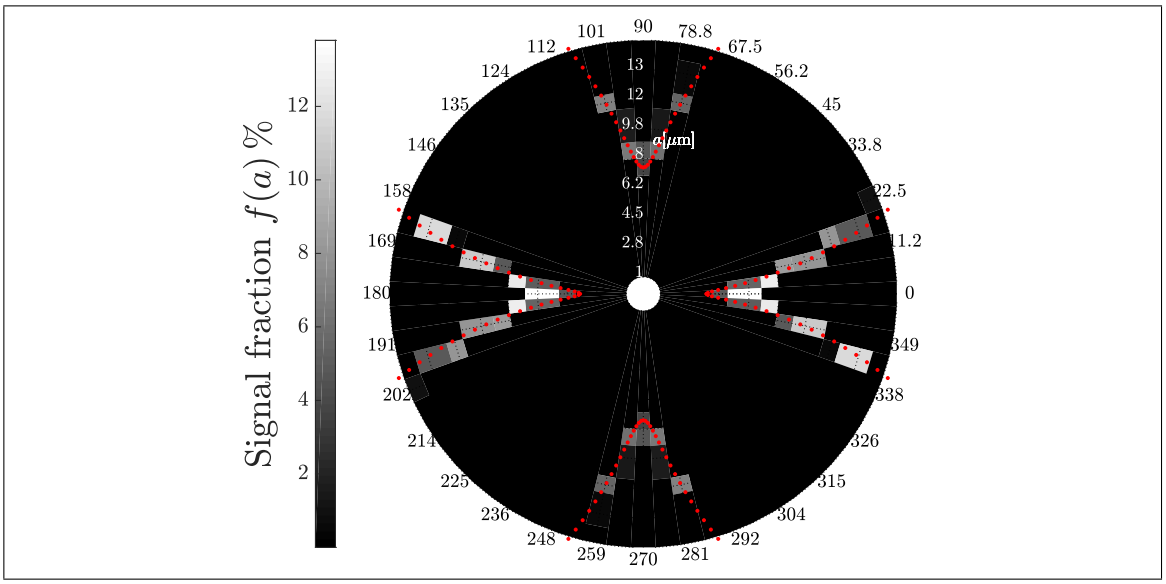

Figure II.4.2. Multiple barrier signal fractions for every direction in a polar grid, where the obtained values are plotted in white and the red dots correspond to the effective barrier approximation stated in Equation II.3.4.

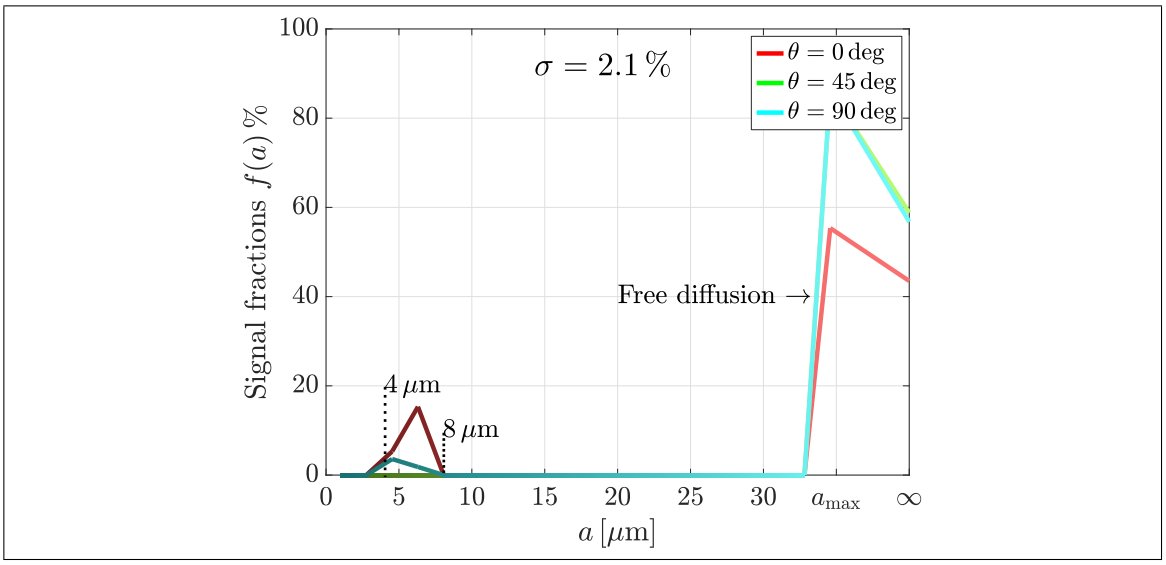

Figure II.4.3. Signal fractions obtained by the proposed method for a noisy signal with noise of $\sigma = 2.1\%$ for multiple diffusion gradient directions as stated in Figure II.3.4. For larger separations the signal is interpreted as noise. The used parameters were $\epsilon = 0.05$, and $\lambda = 10^{-1}$.

In the noisy case, shown in Figure II.4.3, similar results where obtained, but the sensitivity to larger barrier separations decreases due to the noise as in (Sepehrband, Alexander, Kurniawan, et al., 2016). The smaller barriers are less prone to noise if the $q_{\max}$ is big enough.

4.2. Diameter distribution phantom

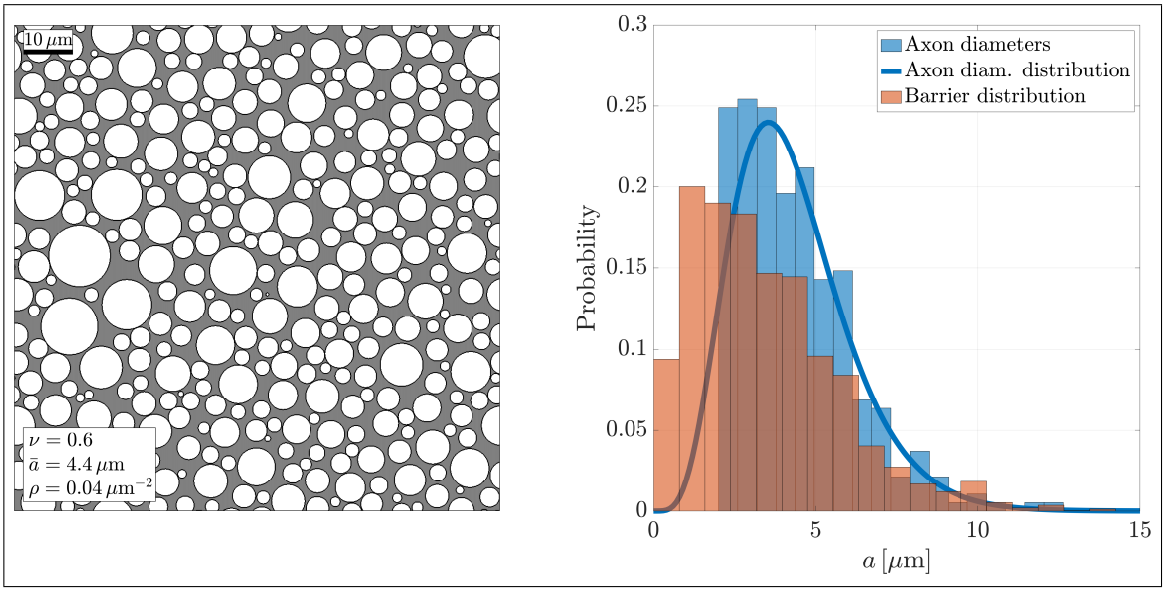

Figure II.4.4. (Left.) Phantom of the corpus callosum, with ν the relation between the area of the axons intra-cellular space and the voxel, $\bar{a}$ the mean diameter and ρ the density of axons. (Right.) Comparison between the obtained axon diameter distribution and the barrier distribution.

In the case of the corpus callosum phantom shown in Figure II.4.4, we averaged the resulting signal fractions in each direction $\bar{\boldsymbol{f}}$ as the microstructure is isotropic in the $q_x - q_y$ plane. This result gave similar results to the correct microstructure for the noiseless and noisy case (Figure II.4.5).

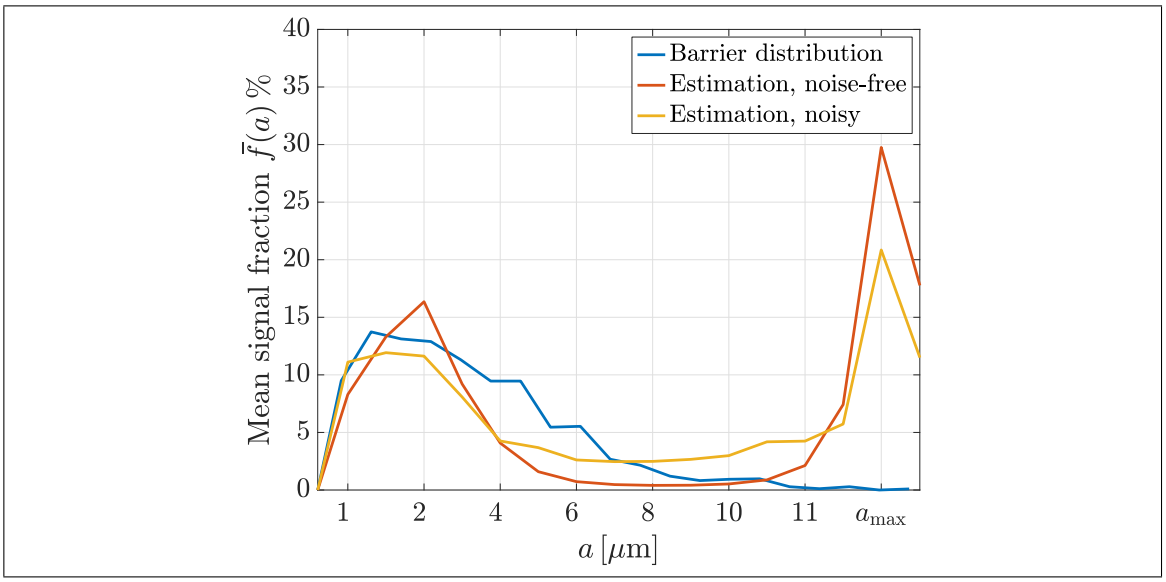

Figure II.4.5. Mean barrier distribution estimated from data, with optimization parameters of $\epsilon = 0.03$ and $\lambda = 5 \cdot 10^{-6}$ for the noise-free case and $\epsilon = 0.14$ and $\lambda = 10^{-2}$ with noise of $\sigma = 5\%$.

While our method estimates well the barrier distribution, it can not differentiate if the signal comes from the intra or extra cellular space. Caution must be used interpreting this results because, depending on the axon density ρ and axon fraction ν, the barrier distribution can lead to underestimations or overestimations to the axon diameter a_{cyl}. This is because a densely packed microstructure have extra cellular spaces with small barriers and the opposite for loosely packed microstructure.

In our case, the ground truth mean axon diameter is $\bar{a}_{\text{cyl}} = 4.4\,\mu\text{m}$ and mean barrier size is $\bar{a} = 3.4\,\mu\text{m}$. The estimated mean barrier size were $4\,\mu\text{m}$ in the noise-free case and $5\,\mu\text{m}$ in the noisy case, giving $\hat{\bar{a}}_{\text{cyl}} = 4.6\,\mu\text{m}$ and $\hat{\bar{a}}_{\text{cyl}} = 5.7\,\mu\text{m}$ respectively, using the method explained in (II.3.6). These values were calculated without considering $a_{\max}$ and the free diffusion signal fractions so

$$\bar{a} = \frac{\sum_{i=1}^{M-2} \bar{f}_i a_i}{\sum_{i=1}^{M-2} \bar{f}_i}.$$

For more parameters as the axon density ρ or axon fraction ν it is necessary to know which signal comes from the intra and extra cellular spaces.

5. CONCLUSIONS

The proposed method was able to find an effective barrier separation which agrees well with the ground truth (available from the simulations). The advantage of this model is that it can be fit with only one diffusion time per shell, and that it does not require geometrical assumptions. In the future, undersampling techniques in order to reduce the number of data points needed and other sparse domains besides the identity could be explored. While not studied, some other types of regularization using angular correlations could improve the results for noisy data as well. In this work we only tested the method with simulated data. Nevertheless, *Ex-vivo* data sets (Assaf et al., 2008; Sepehrband, Alexander, Kurniawan, et al., 2016) can also be used.

An estimation of the axon diameter is possible by being careful on the interpretation of the data, as the signals from the intra and extra cellular spaces cannot be separated by the information available. Thus, errors in the estimations of the axon diameters will occur, but they can still be useful in comparative studies. Additional information about the T_2 decay of the compartments is needed for more accurate results. The sensitivity of microstructure imaging is an ongoing topic of research, and the dependency on the maximum gradient $G_{\max}$, number of shells N and noise levels are important as stated in (Sepehrband, Alexander, Kurniawan, et al., 2016).

In summary our method estimates well the effective barrier separation without requiring extra acquisition time.

REFERENCES

Alexander, D. C., Hubbard, P. L., Hall, M. G., Moore, E. A., Ptito, M., Parker, G. J. M., & Dyrby, T. B. (2010, October). Orientationally invariant indices of axon diameter and density from diffusion MRI. *NeuroImage*, *52*(4), 1374-1389. doi: 10.1016/j.neuroimage.2010.05.043

Assaf, Y., & Basser, P. J. (2005, August). Composite hindered and restricted model of diffusion (CHARMED) MR imaging of the human brain. *NeuroImage*, *27*(1), 48-58. doi: 10.1016/j.neuroimage.2005.03.042

Assaf, Y., Blumenfeld-Katzir, T., Yovel, Y., & Basser, P. J. (2008, June). AxCaliber: A Method for Measuring Axon Diameter Distribution from Diffusion MRI. *Magnetic resonance in medicine*, *59*(6), 1347-1354. doi: 10.1002/mrm.21577

Auría, A., Romascano, D., Canales-Rodriguen, E., Wiaux, Y., Dirby, T. B., Alexander, D., ... Daducci, A. (2015, September). Accelerated microstructure imaging via convex optimisation for regions with multiple fibres (AMICOx). In *2015 IEEE International Conference on Image Processing (ICIP)* (p. 1673-1676). doi: 10.1109/ICIP.2015.7351085

Callaghan, P., MacGowan, D., Packer, K. J., & Zelaya, F. O. (1991, January). Influence of field gradient strength in NMR studies of diffusion in porous media. *Magnetic Resonance Imaging*, *9*(5), 663-671. doi: 10.1016/0730-725X(91)90355-P

Callaghan, P. T. (1993). *Principles of Nuclear Magnetic Resonance Microscopy*. Clarendon Press.

Daducci, A., Canales-Rodríguez, E. J., Zhang, H., Dyrby, T. B., Alexander, D. C., & Thiran, J.-P. (2015, January). Accelerated Microstructure Imaging via Convex

Optimization (AMICO) from diffusion MRI data. *NeuroImage*, *105*, 32-44. doi: 10.1016/j.neuroimage.2014.10.026

Farooq, H., Xu, J., Nam, J. W., Keefe, D. F., Yacoub, E., Georgiou, T., & Lenglet, C. (2016, December). Microstructure Imaging of Crossing (MIX) White Matter Fibers from diffusion MRI. *Scientific Reports*, *6*, 38927. doi: 10.1038/srep38927

Grant, M., & Boyd, S. (2008). Graph implementations for nonsmooth convex programs. In V. Blondel, S. Boyd, & H. Kimura (Eds.), *Recent Advances in Learning and Control* (p. 95-110). Springer-Verlag Limited. (http://stanford.edu/˜boyd/papers/graph_dcp.html)

Grant, M., & Boyd, S. (2014, March). *CVX: Matlab Software for Disciplined Convex Programming, version 2.1.* http://cvxr.com/cvx/.

Hall, M., & Alexander, D. (2009). Convergence and parameter choice for Monte-Carlo simulations of diffusion MRI. *IEEE Transactions on Medical Imaging*, *28*, 1354–1364.

Huang, S. Y., Tobyne, S. M., Nummenmaa, A., Witzel, T., Wald, L. L., McNab, J. A., & Klawiter, E. C. (2016, February). Characterization of Axonal Disease in Patients with Multiple Sclerosis Using High-Gradient-Diffusion MR Imaging. *Radiology*, *280*(1), 244-251. doi: 10.1148/radiol.2016151582

Jeurissen, B., Leemans, A., Tournier, J.-D., Jones, D. K., & Sijbers, J. (2013, November). Investigating the prevalence of complex fiber configurations in white matter tissue with diffusion magnetic resonance imaging. *Human Brain Mapping*, *34*(11), 2747-2766. doi: 10.1002/hbm.22099

Piven, J., Bailey, J., Ranson, B. J., & Arndt, S. (1997, August). An MRI study of the corpus callosum in autism. *American Journal of Psychiatry*, *154*(8), 1051-1056. doi: 10.1176/ajp.154.8.1051

Ritchie, J. M. (1982, December). On the relation between fibre diameter and conduction velocity in myelinated nerve fibres. *Proc. R. Soc. Lond. B*, *217*(1206), 29-35. doi: 10.1098/rspb.1982.0092

Sanguinetti, G., & Deriche, R. (2014, April). Mapping average axon diameters under long diffusion time. In *2014 IEEE 11th International Symposium on Biomedical Imaging (ISBI)* (p. 242-245). doi: 10.1109/ISBI.2014.6867854

Scherrer, B., Schwartzman, A., Taquet, M., Prabhu, S. P., Sahin, M., Akhondi-Asl, A., & Warfield, S. K. (2013). Characterizing the DIstribution of Anisotropic MicrO-structural eNvironments with Diffusion-weighted imaging (DIAMOND). *Medical image computing and computer-assisted intervention (MICCAI): International Conference on Medical Image Computing and Computer-Assisted Intervention*, *16*(0 3), 518-526.

Sepehrband, F., Alexander, D. C., Clark, K. A., Kurniawan, N. D., Yang, Z., & Reutens, D. C. (2016). Parametric Probability Distribution Functions for Axon Diameters of Corpus Callosum. *Frontiers in Neuroanatomy*, *10*. doi: 10.3389/fnana.2016.00059

Sepehrband, F., Alexander, D. C., Kurniawan, N. D., Reutens, D. C., & Yang, Z. (2016, March). Towards higher sensitivity and stability of axon diameter estimation with diffusion-weighted MRI. *NMR in Biomedicine*, *29*(3), 293-308. doi: 10.1002/nbm.3462

Stejskal, E. O., & Tanner, J. E. (1965, January). Spin Diffusion Measurements: Spin Echoes in the Presence of a Time-Dependent Field Gradient. *The Journal of Chemical Physics*, *42*(1), 288-292. doi: 10.1063/1.1695690

Sukstanskii, A. L., Yablonskiy, D. A., & Ackerman, J. J. H. (2004, September). Effects of permeable boundaries on the diffusion-attenuated MR signal: Insights from a one-dimensional model. *Journal of Magnetic Resonance*, *170*(1), 56-66. doi: 10.1016/j.jmr.2004.05.020

Tanner, J. E., & Stejskal, E. O. (1968, August). Restricted Self-Diffusion of Protons in Colloidal Systems by the Pulsed-Gradient, Spin-Echo Method. *The Journal of Chemical Physics*, *49*(4), 1768-1777. doi: 10.1063/1.1670306

Yablonskiy, D. A., & Sukstanskii, A. L. (2010, January). Theoretical models of the diffusion weighted MR signal. *NMR in Biomedicine*, *23*(7), 661-681. doi: 10.1002/nbm.1520

Zhang, H., Schneider, T., Wheeler-Kingshott, C. A., & Alexander, D. C. (2012, July). NODDI: Practical in vivo neurite orientation dispersion and density imaging of the human brain. *NeuroImage*, *61*(4), 1000-1016. doi: 10.1016/j.neuroimage.2012.03.072